

# Generation, dynamics, and correlations of the fission fragments' angular momenta

Guillaume Scamps<sup>1\*</sup>

<sup>1</sup>*Department of Physics, University of Washington, Seattle, Washington 98195-1560, USA*

George Bertsch<sup>2</sup>

<sup>2</sup>*Institute for Nuclear Theory and Department of Physics,  
University of Washington, Seattle, Washington 98195-1560, USA*

The generation of angular momentum in fissioning nuclei is not well understood. The predictions of different models disagree, particularly concerning the correlation between the fragments' angular momenta. In this article, a time-dependent collective Hamiltonian model is proposed to treat the generation of the angular momentum in the fission fragments due to the quantum uncertainty principle as well as the dynamics of the collective wave function during and after scission. The model is constructed in the framework of the frozen Hartree-Fock approximation using a Skyrme energy functional to extract deformations of the fission fragments as well as the interactions in a derived collective Hamiltonian. The fission reactions studied are  $^{240}\text{Pu} \rightarrow ^{132}\text{Sn} + ^{108}\text{Ru}$  and  $^{240}\text{Pu} \rightarrow ^{144}\text{Ba} + ^{96}\text{Sr}$ . The model can account for a large part of the angular momentum found in experimental data. The orientation of the angular momentum of each fragment is found to be mainly in the plane perpendicular to the fission axis, in agreement with the experiment. The magnitudes of the angular momenta in the two fragments are nearly uncorrelated, in agreement with the recent experimental data of Wilson et al., *Nature (London)* 590, 566 (2021). Some of the conclusions of the traditional collective vibration model are supported by the present model but some are not. Surprisingly, it is found that the angular momenta of the fragments are slightly correlated positively as in a wriggling mode. It is also found that the presence of an octupole deformation in a fragment can significantly increase the generated angular momentum.

## I. INTRODUCTION

The generation of angular momentum from fission fragments is a complex phenomenon [1]. Different models have been introduced to calculate contributions to angular momentum including statistical fluctuations [2–5] and the quantum effects visible at scission [6–10]. Recently, the projection method has been used to determine the intrinsic angular distribution in the fission fragments [11–15]. However, these methods do not include quantum fluctuations or correlations between the collective degrees of freedom (see, for example, Ref. [16, 17]).

The models can be separated into two kinds, the ones starting from nucleon degrees of freedom and those starting from collective degrees of freedom. In this article, we explore the dynamic effects in a collective quantum model. Much of the angular momentum generated in fission can be understood with the uncertainty principle. When the fragments are deformed and aligned with the fission axis, the radial orientation exhibits a peak at  $0^\circ$  with a small fluctuation,  $\Delta\theta$ , and that requires a coherent superposition of angular momentum,  $L$ . This polarization is caused by a confining potential before scission. During scission, this confining potential disappears progressively. If scission occurs quickly, angular momentum distribution will remain unchanged. However, if scission occurs slowly, the evolution will be adiabatic. Therefore, it is essential to incorporate a realistic treatment of the dynamics to calculate the evolution of the angular

momentum during scission and the Coulomb excitation phase. Indeed, during and after scission, the axes of deformation may be tilted with respect to the fission axis. They are then subjected to the quantum equivalent of the classical torque due to the Coulomb<sup>1</sup> interaction [9, 18–22].

The present article proposes a model to describe the time-dependent evolution based on a realistic interaction acting on the wave function of the orientation angles. The goal is to understand the fluctuations in the angular properties of the post-fission fragment. This approach is similar to the Density-Constrained Hartree-Fock (Bogoliubov) [23–26] or Frozen Hartree-Fock (FHF) approximations [27, 28], which have been used to model accurately fusion tunneling. The model does not include the angular momentum associated with quasiparticle excitations and so assumes that the fragments are cold and rigid. However, it goes beyond previous microscopic approaches in that it treats explicitly the rotational collective degrees of freedom as well as their correlations.

The article is organized as follows. In Sec. II we present the collective Hamiltonian model and its ingredients. In Sec. III, the distributions of fragment angular momenta are presented. The correlations between the angular momenta of the fragments are discussed in Sec. IV. Sec. V A discusses the sensitivity to parameters in the model. Sec. VI discusses the contribution of octupole deformation for the fission fragment  $^{144}\text{Ba}$ .

\* gscamps@uw.edu

<sup>1</sup> See the torque formulation in Appendix C.

## II. METHOD

### A. Collective coordinates of the fissioning systems

The model consists of two cold fragments separated by a distance  $D$  along the  $z$ -axis, which is treated as the fission axis. The fragments are oriented with their principal deformation axes forming an angle  $\theta$  with the  $z$ -axis and an azimuthal angle  $\varphi$  with respect to the  $x$ -axis as shown in Fig. 1.

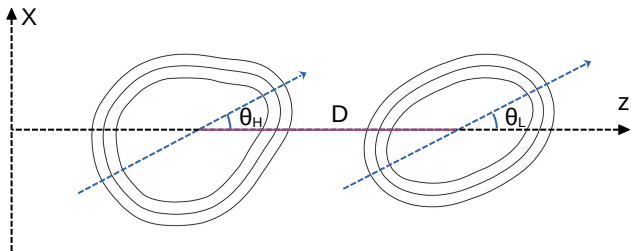


Figure 1. Schematic view of the model in the  $x$ - $z$  plan in the case of  $\varphi_H=0$  and  $\varphi_L=0$ . The blue dashed line shows the principal axis of deformation of each fragment.

To construct the collective Hamiltonian, the FHF method with the Sly4d interaction [29] described in a previous study (Ref. [22]) will be employed to calculate the interaction potential between the fragments as a function of  $D$  and the angular variables. We treat two fission reactions:  $^{240}\text{Pu} \rightarrow ^{132}\text{Sn}+^{108}\text{Ru}$  and  $^{240}\text{Pu} \rightarrow ^{144}\text{Ba}+^{96}\text{Sr}$ . The two mass splittings produce fragments of quite different shapes. The deformation is large for  $^{108}\text{Ru}$ , moderate for  $^{96}\text{Sr}$ , and vanishes for the doubly magic  $^{132}\text{Sn}$ . The  $^{144}\text{Ba}$  has a large octupole deformation that turns out to have a significant role. Due to its spherical shape, and the assumption that fragments are cold, the experimental spin of the  $^{132}\text{Sn}$  cannot be described in our model.

Table I. Deformations of the four nuclei considered in this study, calculated from the self-consistent ground state or superdeformed minimum as described in the text. The last column gives the rigid moment of inertia on an axis perpendicular to the deformation axis of the nucleus. All fragments are found to be axially symmetric.

Nuc.	$\beta_2$	$\beta_3$	$\beta_4$	$E^*$ [MeV]	$I_{\text{Rigid}}$ [ $\hbar^2/\text{MeV}$ ]
$^{132}\text{Sn}$	0.	0.	0.	0	50.0
$^{108}\text{Ru}$	0.82	0.	0.71	3.5	51.4
$^{144}\text{Ba}$	0.22	0.16	0.15	0	63.1
$^{96}\text{Sr}$	0.53	0.	0.25	0	37.1

Except for  $^{108}\text{Ru}$ , the fragment deformations in the model are obtained from their calculated density distributions as isolated nuclei in their ground states.  $^{108}\text{Ru}$  is likely to be produced in a super-deformed minimum, and we make that assumption. The  $\beta$  values are shown

in Table I, using the definition<sup>2</sup>

$$\beta_\ell = \frac{4\pi}{3A(r_0 A^{1/3})^\ell} Q_{\ell 0} \sqrt{\frac{2\ell+1}{16\pi}}, \quad (1)$$

$$Q_{\ell 0} = \int d^3\mathbf{r} \rho(\mathbf{r}) r^\ell \sqrt{\frac{16\pi}{2\ell+1}} Y_{\ell,0}(\theta, \varphi), \quad (2)$$

with  $r_0 = 1.2$  fm. The Hamiltonian also depends on the fragments' moments of inertia. Most of the calculations described below use the rigid values shown in Table I, computed as

$$I_{\text{Rigid}} = m \int d^3\mathbf{r} \rho(\mathbf{r}) (x^2 + y^2). \quad (3)$$

The quantum degrees of freedom in the model are the orientation angles of the fragments, while the separation coordinate between the fragments is treated as an external time-dependent parameter. For a full treatment of the angular momentum in the system, one would also include the orientation of the fission axis as another degree of freedom. We assume that the system as a whole has angular momentum zero in which case the fission axis rotation is not an independent degree of freedom (see App. D).

If one of the fragments is spherical, rotational invariance permits a Hamiltonian with only one internal angular momentum variable, namely the angle between the fission axis and the axis of the deformed fragment. When both fragments are deformed, the Hamiltonians depend on three angular variables, namely the two deformation axes  $\theta_L$  and  $\theta_H$  and the azimuthal angle  $\varphi = \varphi_H - \varphi_L$  between them.

### B. Model Hamiltonian

#### 1. Single-angle model

As mentioned above, the  $^{132}\text{Sn}+^{108}\text{Ru}$  fission reaction can be treated with a single-angle Hamiltonian. We write this as

$$\hat{H}(D) = \frac{\hbar^2}{2} \left( \frac{1}{I} + \frac{1}{I_\Lambda(D)} \right) \left( \frac{1}{\sin(\theta)} \frac{\partial}{\partial \theta} \left( \sin(\theta) \frac{\partial}{\partial \theta} \right) \right) + V(\hat{\theta}, D) \quad (4)$$

where the interaction  $V(\hat{\theta}, D)$  includes both nuclear and Coulomb terms. The rotational energy has two terms;  $I$  is the inertia of the fragment given in Table I and  $I_\Lambda = m \frac{A_H A_L}{A_H + A_L} D^2$  is the inertia of the fragments about

<sup>2</sup> Note that the present definition of  $Q_{\ell 0}$  differs by a factor 2 from the conventional formula for  $\ell \neq 2$

the system's center of mass. The Hamiltonian can be equivalently written in the angular momentum basis,

$$H_{LL'}(D) = \frac{\hbar^2}{2} \left( \frac{1}{I} + \frac{1}{I_\Lambda(D)} \right) L(L+1)\delta_{LL'} + V_{LL'}(D), \quad (5)$$

which is more convenient to calculate. The interaction is transformed to the angular momentum basis by

$$V_{LL'}(D) = \int_0^\pi \sin(\theta) V(\theta, D) P'_L(\cos(\theta)) P'_{L'}(\cos(\theta)) d\theta, \quad (6)$$

using the Legendre polynomial basis  $P'_L(\theta)$  normalized such that,  $\int_0^\pi \sin(\theta) P'_L(\cos(\theta))^2 d\theta = 1$ . The potential  $V(\theta, D)$  is determined in the Frozen Hartree-Fock approximation (See Appendix A). It takes into account the long-range Coulomb potential and the short-range nucleus-nucleus interaction. The Hamiltonian is computed in a basis truncated at  $L_{\max} = 40 \hbar$ . The integration on Eq. (6) is done with the simple trapezoidal rule with  $\Delta\theta = \pi/500$ .

## 2. Triple-angle model

When both fragments are deformed, as in the  $^{240}\text{Pu} \rightarrow ^{144}\text{Ba} + ^{96}\text{Sr}$  case, three angles need to be specified for the fragment orientation as mentioned in Sec. IIA. These correspond to three quantum numbers in the angular-momentum basis states  $|L_H, m, L_L, -m\rangle$ , namely  $L_H$  and  $L_L$  for the principal quantum numbers of the fragments and  $\pm m$  for the azimuthal quantum numbers. The total azimuthal angular momentum is zero in the starting wave function (by assumption) and remains unchanged during the Schrödinger evolution. The basic model assumption is again to treat the fission fragments as rigid rotors using the distance  $D$  between the fragments as a time-dependent parameter of the Hamiltonian. The collective Hamiltonian can then be written,

$$\hat{H}(D) = \frac{\hbar^2}{2I_H} \hat{L}_H^2 + \frac{\hbar^2}{2I_L} \hat{L}_L^2 + \frac{\hbar^2}{2I_\Lambda(D)} \hat{\Lambda}^2 + \hat{V}(D), \quad (7)$$

with  $\hat{\Lambda} = -\hat{L}_H - \hat{L}_L$  the orbital angular momentum of the fragments about the center of mass. The parameters  $I_H$  and  $I_L$  are the moment of inertia (MOI) associated with the rotors and  $I_\Lambda(D)$  is the MOI associated with the angular momentum about the center of mass. The nucleus-plus-Coulomb potential  $V(\hat{\theta}_H, \hat{\theta}_L, \hat{\varphi}, D)$  (See Appendix B) is calculated by the FHF approximation as a function of orientation angles and then converted in the  $|L_H, L_L, m\rangle$  basis defined as,

$$|L_H, m, L_L, -m\rangle = \int_0^\pi d\theta_H \int_0^\pi d\theta_L \int_0^{2\pi} d\varphi_H \int_0^{2\pi} d\varphi_L \sin(\theta_L) \sin(\theta_H) P'_{L_H, m}(\cos(\theta_H)) P'_{L_L, -m}(\cos(\theta_L)) e^{im(\varphi_H - \varphi_L)} |\theta_H, \varphi_H, \theta_L, \varphi_L\rangle. \quad (8)$$

with  $P'_{l, m}(x)$  the associated Legendre polynomials with the appropriate normalisation.

The operator  $\hat{\Lambda}^2$  can be written in the  $|L_H, L_L, m\rangle$  basis,

$$(\Lambda^2)_{L_H, L_L, m, L'_H, L'_L, m'} = \delta_{L_H, L'_H} \delta_{L_L, L'_L} \left( \delta_{m, m'} (L_H(L_H + 1) + L_L(L_L + 1) - 2m^2) + \delta_{m, m'+1} \sqrt{(L_H(L_H + 1) - m(m-1))(L_L(L_L + 1) - m(m-1))} + \delta_{m, m'-1} \sqrt{(L_H(L_H + 1) - m(m+1))(L_L(L_L + 1) - m(m+1))} \right). \quad (9)$$

Numerically, the space includes states with  $L$  up to  $30\hbar$  and  $|m| \leq 2\hbar$ , which gives a total number of states of 4443. It has been checked that the results are unaffected by increasing the size of the basis.

## C. Schrödinger dynamics

The system is evolved with the time-dependent Schrödinger equation,

$$i\hbar \frac{d}{dt} \Psi(t) = \hat{H}(D(t)) \Psi(t) \quad (10)$$

taking  $D(t)$  from time-dependent Hartree-Fock (TDHF) calculation in Ref. [22]. The starting point at  $t = 0$  is the ground eigenstate of the Hamiltonian at a separation

distance  $D_0$ , obtained by a direct diagonalization of the Hamiltonian in the angular momentum basis. For most of the calculations reported here we take  $D_0 = 14$  fm. This was chosen as the closest point where the potential favors an aligned orientation of the rotors along the fission axis.

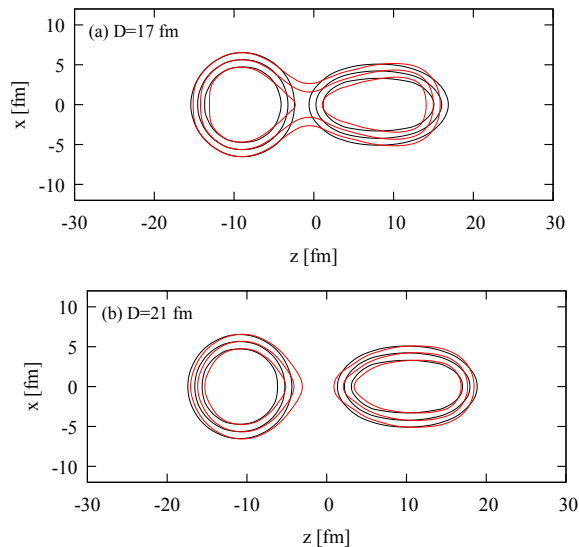


Figure 2. (Color online) Comparison between the static (black curves) and dynamical shapes obtained respectively by the FHF and TDHF calculations in the  $^{240}\text{Pu} \rightarrow ^{132}\text{Sn} + ^{108}\text{Ru}$  case.

The evolution of the wave packet  $\Psi(t)$  is obtained by solving Eq. (10) with the Runge-Kutta method at the order 4 with a time step  $\Delta t = 0.25$  fm/c. It has been checked that the final results were unaffected by a change to a smaller value of  $\Delta t$ . The wave function is evolved until  $D(t) = 100$  fm, which is sufficient to have a complete convergence of the final angular momentum distribution.

We found two problems with a naive use of the FHF nuclear interaction due to the limited characterization of the nuclear shapes in the model. The first one is just an annoyance arising from the invariance of the fragment density under the parity transformation when only even moments of the density are present. In that case, a pocket in the potential at  $\theta = 0$  will be accompanied by an identical pocket at  $\theta = \pi$ . This gives an unwanted near-degeneracy of the eigenstates. We deal with this by setting the nuclear part of  $V(D)$  beyond  $\theta = \pi/2$  its value at  $\pi/2$ .

The second problem arises from the lack of explicit neck degrees of freedom in the collective model. During scission, the TDHF evolution proceeds through an elongation as well as a narrowing of the neck. This gives rise to very high multipole deformations in the newly formed fragments. The FHF Hamiltonian lacks those neck degrees of freedom, as may be seen in Fig. 2 comparing the density distributions at  $D = 17$  fm. The extended neck produces a stronger nuclear attraction between the nascent fragments than the FHF Hamiltonian provides.

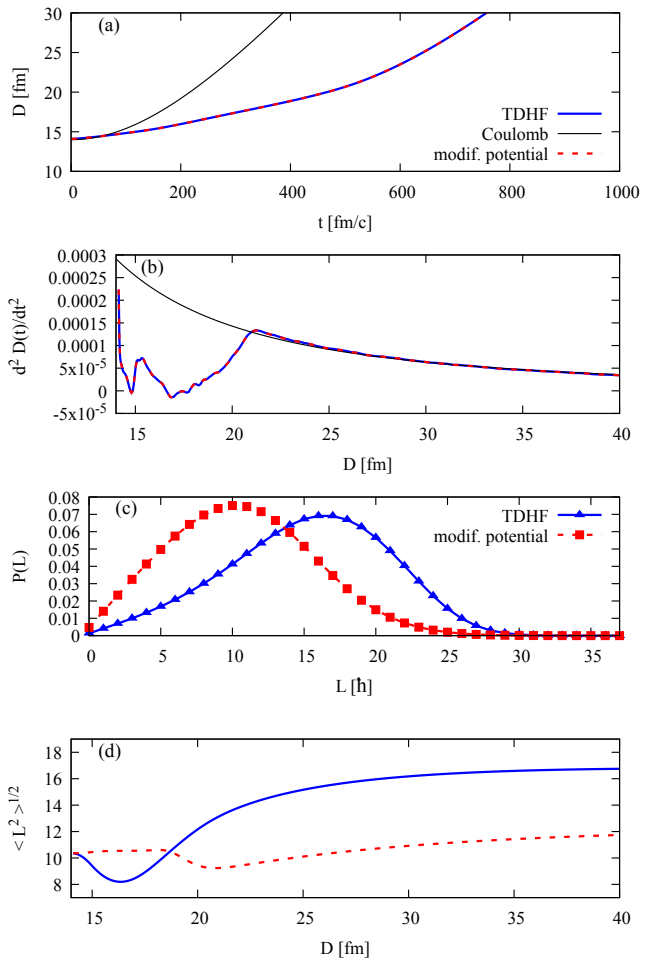


Figure 3. (Color online) Evolution of  $D$  and angular momentum in the fission reaction  $^{240}\text{Pu} \rightarrow ^{132}\text{Sn} + ^{108}\text{Ru}$ . a) Distance between the center of mass of the fragments as a function of time. b) Acceleration of the fragments. c) Final distribution of spin. d) Evolution of the average angular momentum as a function of the distance between the fragments. Different assumptions are made here: i) A TDHF evolution of  $D(t)$  (blue curve), ii) a pure Coulomb repulsion from  $D=14$  fm (black thin curve) iii) a TDHF evolution up to  $D_{sc}=17$  fm and pure Coulomb repulsion afterward iv) a TDHF evolution but the NN potential  $V(\theta, D)$  is modified with  $D \rightarrow D + 4$  fm (red dashed curve).

We take this into account by displacing the FHF nuclear potential in the  $D$  coordinate.

The distance to shift the FHF potential is determined by matching the final scission point as found in the TDHF calculation. For the TDHF calculation, we take that as the point in the dynamic evolution where the acceleration of the fragments is maximal. From Fig. 3(b), this occurs near  $D = 21$  fm. For the FHF Hamiltonian, we take the final scission point at the separation  $D$  where the confinement to small orientation angles disappears, ie.

$$\frac{d^2 V_D(\theta)}{d\theta^2} \Big|_{\theta=0} = 0. \quad (11)$$

That point is at  $D = 17$  fm, 4 fm closer. This is consistent with many other fission models [30–34], locating the scission point several fm beyond what one would calculate in the frozen approximation. The shift is incorporated in our modified FHF  $V'$  as follows:

$$V'_{NN}(D) = V_{NN,FHF}(D - 4) \quad \text{for } D \geq D_0 + 4 \text{ fm}, \quad (12)$$

$$V'_{NN}(D) = V_{NN,FHF}(D_0) \quad \text{for } D < D_0 + 4 \text{ fm}. \quad (13)$$

with  $D_0 = 14$  fm. We find that the modified interaction reduces the generation of angular momentum (See Fig. 3). This is because stronger nuclear interaction acts against the Coulomb interaction in the region  $17 \text{ fm} < D < 21 \text{ fm}$ .

### III. CALCULATED ANGULAR MOMENTUM OF THE FISSION FRAGMENTS

#### A. Angular momentum in the one-angle model

In the case of the  $^{240}\text{Pu} \rightarrow ^{132}\text{Sn} + ^{108}\text{Ru}$  fission, the  $^{132}\text{Sn}$  fragment is spherical in the FHF approximation and  $V(D)$  depends only on  $\theta_L$ , the orientation angle of the light fragment. The initial probability distribution at  $D=14$  fm is shown in Fig. 4 in the orientation (panel (a)) and angular momentum basis (panel (b)). The stiff initial potential shown on panel (c) confines the wave function in the small angle region around  $\theta_L=0$ . The strongly oriented wave function must include high angular momentum components due to the uncertainty principle [7, 35]. This initialization is similar to the model of ref. [7–10, 20]. However, the present model is based on a realistic microscopic potential and does not rely on a small angle approximation.

The evolution of the probability distribution in the one-angle case is shown in Fig. (4b). Before scission, the confining pocket at small angles becomes softer and softer; the wave packet expands a bit, reducing the average angular momentum. After the scission at  $D=21$  fm the wave packet spreads toward  $\theta_L=90^\circ$  due to the kinetic terms in the Hamiltonian as seen in Fig. (4a) and the Coulomb torque generates additional angular momentum (see Sec. C). The final angular momentum is obtained from the wave function at  $D(t) = 100$  fm.

#### B. Triple-angle calculation

The case where both fragments are deformed presents a more rich dynamics with the possibility of correlation between the two angular momenta. But first, we determine the angular momentum distribution of each fragment.

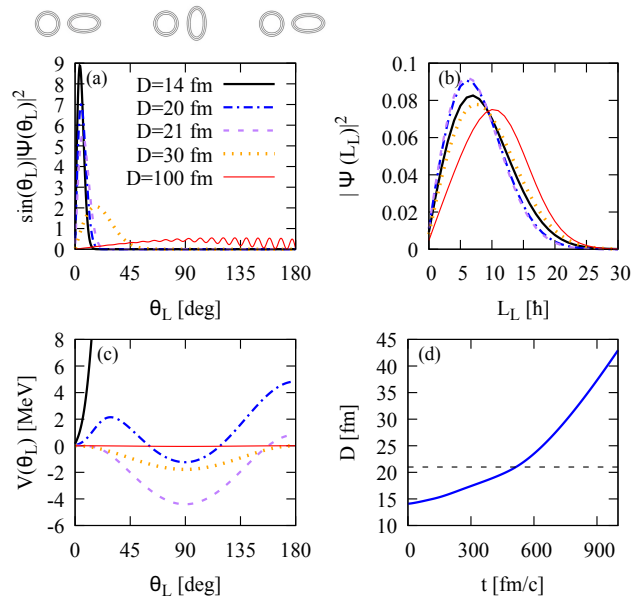


Figure 4. (Color online) (a) Angular wave function describing the orientation of the  $^{108}\text{Ru}$  light fragment at different distances  $D$ . The  $^{132}\text{Sn}$  complementary fragment is assumed to be spherical. (b) Snapshot of the angular momentum distribution at different times. (c) Angular potential in which the wave function is evolved. (d) Evolution  $D(t)$  obtained from the TDHF calculation (blue solid curve), the dashed line shows the distance for which the acceleration of the fragment is the maximum. Above panel (a) a schematic figure shows the orientation of the light fragment as a function of the angle  $\theta_L$ .

The angular momenta of the fragments are shown in Fig. 5 at the initial distance and at the final one. The angular momentum distribution seen in the light fragment is found to be smaller than in the heaviest one. It will be shown in Sec. VI that it is due to the octupole deformation in the heavy fragment.

To see if the distribution obtained by the collective Hamiltonian model deviates from the Bethe formulae, the figure shows a comparison between the spin-cutoff formulae,

$$P(L) \propto (2L + 1)e^{-\frac{L(L+1)}{(2\sigma^2)}}, \quad (14)$$

and the initial and final spin distribution. A good agreement is found with the formulae for the initial distribution, but dynamics change the shape of the distribution. Especially for the light fragment which is more affected by the Coulomb torque.

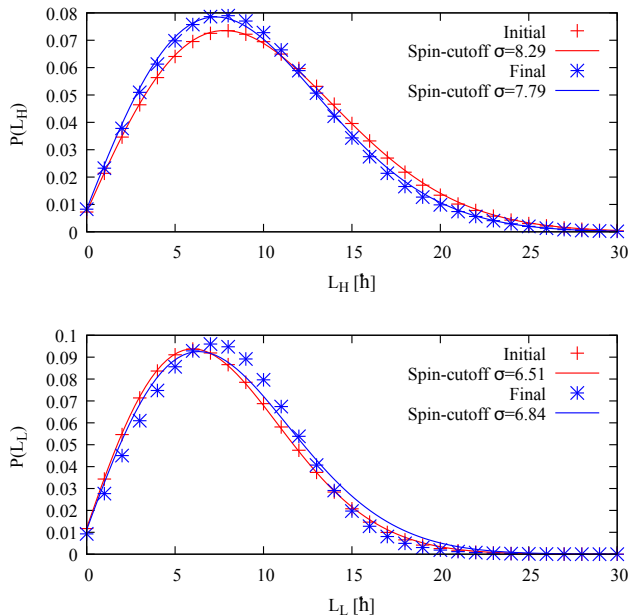


Figure 5. (Color online) Initial and final spin distributions of the heavy (top) and light (bottom) fragments in the fission reaction  $^{240}\text{Pu} \rightarrow ^{144}\text{Ba} + ^{96}\text{Sr}$ . Solid lines show the comparison to Eq. (14).

#### IV. ANGULAR MOMENTUM CORRELATIONS

##### A. Correlation between the magnitudes of the angular momenta

The reaction  $^{240}\text{Pu} \rightarrow ^{144}\text{Ba} + ^{96}\text{Sr}$  is interesting for examining the correlations between the fragment's angular momenta since both are deformed. The two-dimensional probability distribution of angular momentum magnitudes  $P(L_H, L_L) = \sum_m |\Psi(L_H, L_L, m)|^2$  is shown in panel (a) of Fig. 6. There is hardly any correlation between the two magnitudes. For a quantitative measure, panel (b) shows the average angular momentum of one of the fragments as a function of the other,

$$\begin{aligned} \langle \hat{L}_L^2 \rangle_{L_H} &= \frac{\sum_{L_L} L_L(L_L + 1)P(L_H, L_L)}{\sum_{L_L} P(L_H, L_L)}, \\ \langle \hat{L}_H^2 \rangle_{L_L} &= \frac{\sum_{L_H} L_H(L_H + 1)P(L_H, L_L)}{\sum_{L_H} P(L_H, L_L)}. \end{aligned} \quad (15)$$

One sees only a small correlation between the magnitude of the angular momentum of the fragments. The angular momentum of the heavy fragment varies by about one unit depending on the light fragment. This result is compatible with the experimental data of ref. [36].

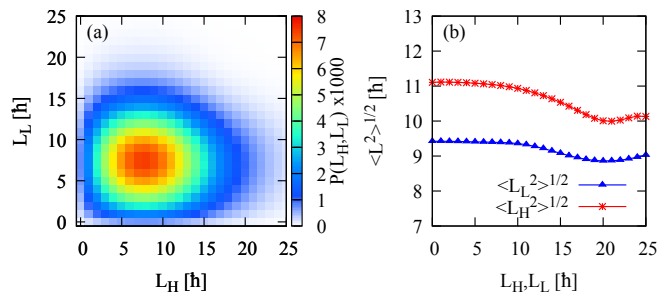


Figure 6. (Color online) (a) Distribution of the angular momentum of the heavy and light fragment. (b) Average angular momentum of one of the fragments as a function of the angular momentum of the other fragment.

##### B. Correlation between the orientations of the angular momenta

We describe here the different types of correlations, based on the nomenclature of the modes. These modes have been introduced in models that assume the fragments rotate in a strongly correlated way as in a rigid classical model. However, in the present model, we describe the system with a collective wave packet that describes soft correlations between the orientation of the two fragments' angular momenta. The three types of correlations described in the following are shown in Fig. 7. The correlations of the orientation of the angular momenta are described as bending when the spins are in the same direction and in the plane perpendicular to fission, wriggling when they are in opposite directions, and twisting when the angular momenta are aligned in the fission axis. Tilting is ignored in this figure since it is a forbidden mode in our model due to the assumption that the total angular momentum is zero. In practice, our model mixes the three kinds of correlations with a wave packet describing the directions of the angular momenta.

Although the magnitudes of the angular momenta are uncorrelated (see Sec. IV A), there is a substantial correlation between their directions. As early studies have shown [19], both angular momenta are largely perpendicular to the fission axis. This implies that  $m = 0$  is favored in the angular momentum representation; in the present model the probability of  $m \neq 0$  is of the order of 1% (see Fig. 8(b)). This affects the angular correlation with respect to the relative azimuthal angle between the two fragments  $\varphi = \varphi_H - \varphi_L$ .

Although the non-zero  $m$  components are small, there are visible correlations in the black curve in Fig. 8(a). The configuration with relative azimuthal angle  $\varphi = 180^\circ$  is two times more probable than the one with  $\varphi = 0^\circ$ .

As can be seen in Fig. 15 in Appendix B, the lowest energy configuration is obtained for  $\varphi = 180^\circ$  which corresponds to a shape in V. This correlation arises from the nuclear interaction between the two fragments. At the scission point, the correlation is suppressed, resulting in the disappearance of non-zero  $m$  components. However,

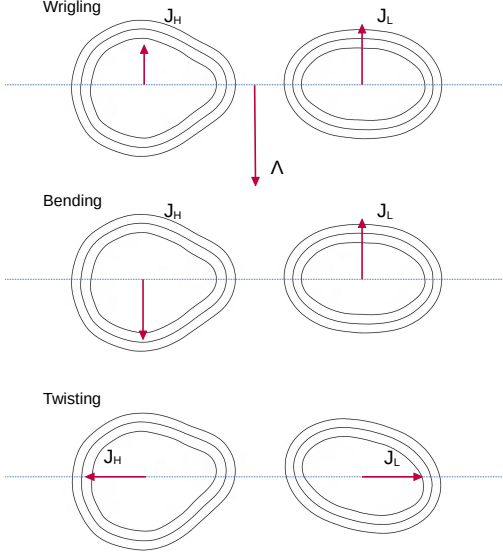


Figure 7. (Color online) Schematic description of the type of correlation between the two fission fragments' angular momenta. The red arrow represents the angular momentum of the fragments.

during the separation phase, the magnitudes of the non-zero  $m$  components increase (See Fig. 8(b)) due to the coupling induced by the  $\Lambda^2$  term in the Hamiltonian (Eq. (7)). Despite this, the  $m = 0$  states continue to largely dominate, which is consistent with the experimental data from Ref. [19].

### C. Opening angle

Recently, the distribution of opening angle  $\varphi_{HL}$  between the fragments' angular momentum vectors has been much discussed. This distribution differs in the various models [4, 5, 14, 37, 38]. We define the distribution as the operator with diagonal elements in the  $|L_H, L_L, \Lambda, M\rangle$  basis

$$\varphi_{HL} = \arccos \left( \frac{\Lambda(\Lambda + 1) - L_H(L_H + 1) - L_L(L_L + 1)}{2\sqrt{L_H(L_H + 1)L_L(L_L + 1)}} \right) \quad (16)$$

and zero off-diagonal elements. Its probability distribution is obtained from the distribution of states  $|L_H, L_L, \Lambda\rangle$ .

$$P(\varphi_{HL}) = \sum_{\substack{\Lambda, L_H > 0, \\ L_L > 0}} \delta(\varphi_{HL} - \varphi_{HL}(\Lambda, L_H, L_L)) \left| \sum_m (L_H, m, L_L, -m | \Lambda, 0) \Psi(L_H, m, L_L, -m) \right|^2.$$

This formula is similar to the semi-classical formula

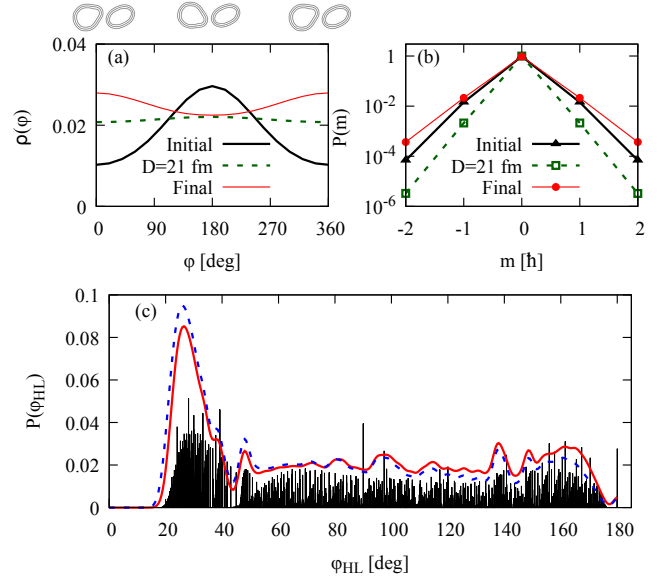


Figure 8. (Color online) Angular momentum correlations in the fission reaction (a) Distribution of the relative azimuthal angle  $\varphi$  (describing the spatial orientation of the fragments), at the initial time, scission, and large distance. The corresponding configuration is shown above the figure. (b) Distribution of the projection of the angular momentum on the fission axis. (c) Final distribution (unnormalized) in an arbitrary unit of the opening angle between angular momenta computed as Eq. (16) (black bar). The distribution averaged with a  $2^\circ$  wide Gaussian function is shown with a red line. The dashed blue line shows the initial distribution.

in Ref. [14, Eq. (4)]. To replace  $\sqrt{L_{H,L}(L_{H,L} + 1)}$  by  $L_{H,L} + 1/2$  leads to a very similar distribution. Note that the value of  $\varphi_{HL}$  is fixed by the quantum numbers of component  $|L_H, L_L, \Lambda\rangle$ , so the probability distribution is a set of discrete spikes. Fig. 8 shows that distribution. It has a large concentration of strength near  $25^\circ$  associated with the states in which  $\Lambda = L_H + L_L$ . The average angle is found to be  $86.7^\circ$  ( $78.4^\circ$  for the initial distribution). None of the models described in ref. [4, 5, 14, 37] has this feature. In the language of the collective vibrational models, these values would correspond to the presence of a wrigling mode. This distribution is close to the one found in time-dependent density functional theory [39], with the difference that the distribution of  $K$  in the microscopic approach diminishes the peak at small opening angles.

### D. Correlation in a direction perpendicular to the fission axis

To determine the degree of alignment of the angular momenta, the correlated wave function is projected in the basis  $|L_H, L_{Hx}, L_L, L_{Lx}\rangle$ . This enables the calculation of the correlation between the angular momentum projected

on a transverse axis (called "x"):

$$P(L_{Hx}, L_{Lx}) = \sum_{L_H, L_L} |\Psi(L_H, L_{Hx}, L_L, L_{Lx})|^2. \quad (17)$$

To compute the correlation between the spin in the x direction, the angular momentum basis  $L, m_z$  is turned

$$\Psi_x(L_H, L_{Hx}, L_L, L_{Lx}) = \sum_{L_{Lz}, L_{Hz}} \mathcal{D}_{L_{Hx}, L_{Hz}}^J(0, \pi/2, 0) \mathcal{D}_{L_{Lx}, L_{Lz}}^J(0, \pi/2, 0) \Psi(L_H, L_{Hz}, L_L, L_{Lz}) \quad (18)$$

with Wigner D-function  $\mathcal{D}_{M, M'}^J(\alpha, \beta, \gamma)$ . The two-dimensional probability plot is shown in Fig. 9. The angular momenta are correlated initially, but the correlation is much reduced in the final state. The correlation coefficient  $r_{L_{Hx}, L_{Lx}} = \frac{\text{Cov}(L_{Hx}, L_{Lx})}{\sigma_{L_{Hx}} \sigma_{L_{Lx}}}$  is 0.22 initially and 0.06 at the final time. The positive sign of the coefficient indicates the presence of a wriggling correlation type as opposed to a bending type in the vibrational model. The probability that both projections on the x-axis have the same sign gives the population of the wriggling mode and is found to be 0.58 initially and 0.53 at the end of the evolution.

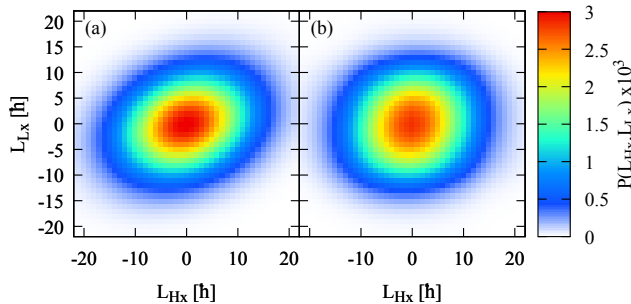


Figure 9. (Color online) Correlations between the projections of the angular momentum on the x-axis at initial (a) and final (b) times.

This may seem to contradict the  $\varphi$  correlation of the rotors' axes that peak at zero as in a bending mode. The reason for this apparent contradiction is as follows: while the potential may favor a V-shaped configuration, the angular momenta of the fragments actually originate from their zero-point motion. Since the confining potential is stiffer in the direction of  $\theta_H - \theta_L$  than in the direction of  $\theta_H + \theta_L$ , the wriggling mode ends up dominating. This result highlights the importance of considering the collective Hamiltonian as a function of all the orientation angles in understanding the angular momentum modes of fission fragments.

by 90 degrees in the y direction. The coefficients in the turned basis are,

Table II. Average spin  $\langle L^2 \rangle^{\frac{1}{2}}$  in unit of  $\hbar$  for the 3 fission fragments at scission ( $D = 21$  fm) and at large distances. The last two columns show the same quantity with an MOI divided by 2.

Nucleus	Scission	Final	Scission ( $I_{\frac{1}{2}}$ )	Final ( $I_{\frac{1}{2}}$ )
$^{108}\text{Ru}$	9.28	12.31	7.24	10.38
$^{144}\text{Ba}$	10.04	10.95	7.70	8.66
$^{96}\text{Sr}$	7.74	9.30	6.03	7.62

## V. PARAMETER SENSITIVITIES

### A. Moment of inertia

So far, we have assumed a rigid-body moment of inertia (MOI) in Eq. (7). The empirical moments are smaller by as much as a factor of two due to pairing effects [40]. To estimate the impact of a different MOI, calculations have been performed with the MOI divided by two. Results are shown in Fig. 11 and Table II. We see that a smaller MOI reduces the average spin in both the initial and final distribution by about  $2\hbar$ .

The reduction occurs already in the initial angular momentum associated with the starting wave function. This is in accord with the qualitative argument in Ref. [7] which discusses the angular localization produced by an attractive pocket in the nuclear potential between the post-scission fragments. The average angular momentum was predicted to scale as  $I^{1/4}$ ; the numerical results in Table II are close to that with a slightly stronger dependence.

The angular momentum generated in the post-scission evolution ranges from 1 to 3 units, and is quite independent of the MOI. An analysis of the quantum mechanics of that process is given in Appendix C, showing that it depends strongly on the dephasing of the components of the wave function in the angular-momentum representation. While the inertial dynamics can contribute to the dephasing, other dephasing mechanisms apparently dominate.

The average final angular momentum for the Hamiltonian with a reduced MOI is in the range 7.5-10.5 $\hbar$ , signif-



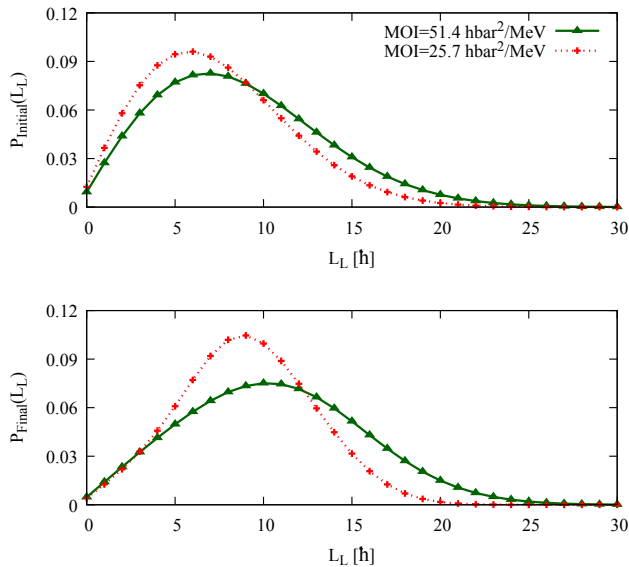


Figure 10. (Color online) Effect of the moment of inertia in the initial (top) and final (bottom) angular momentum distribution in the  $^{108}\text{Ru}$  fission fragment.

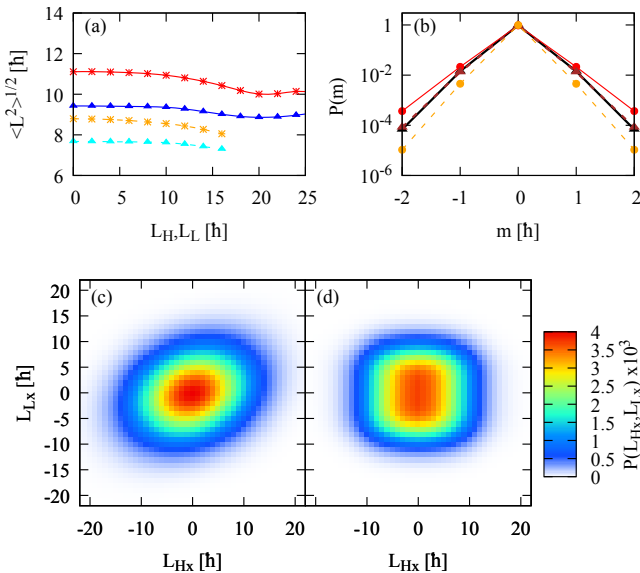


Figure 11. (Color online) Effect of the moment of inertia on the angular momentum correlation in the fission reaction  $^{240}\text{Pu} \rightarrow ^{144}\text{Ba} + ^{96}\text{Sr}$ . (a) Average angular momentum of one (heavy fragment is shown with crosses and light fragment with triangles) of the fragments as a function of the angular momentum of the other fragment for the rigid moment of inertia (solid line) and half the moment of inertia (dashed line). (b) Distribution of  $m$  at the initial (triangles) and final time (dots) for the rigid moment of inertia (solid line) and half the moment of inertia (dashed line). Panels (c) and (d) show the correlations between the angular momentum projected on the x-axis respectively at the initial and final time in the case of the half rigid moment of inertia.

ificantly higher than the experimental values for comparable nuclei [36]. This could be due to model limitations or angular momentum carried by emitted neutrons [12, 41].

## B. Choice of $D_0$

The choice of the point to start the Schrödinger evolution is not well determined, since the dynamics of the neck elongation and thinning are beyond the scope of the model. We chose  $D_0 = 14$  fm as a point where the two proto-fragments overlap but the scission has proceeded enough to where the mass splitting between them is clear. To get an idea of the model uncertainty of this parameter we have also analyzed cases with larger values of  $D_0$ . Ini-

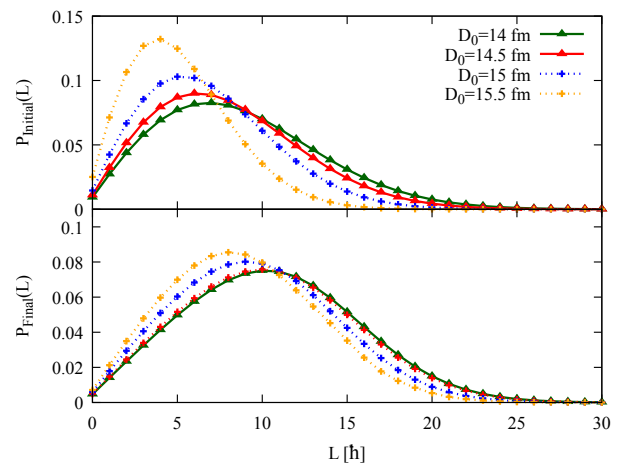


Figure 12. (Color online) Distribution of  $L_L$  at  $t=0$  (top) and final time (2nd panel) for different values of  $D_0$  in the  $^{132}\text{Sn} + ^{108}\text{Ru}$  case.

tial and final distributions for the range  $D_0 = 14 - 15.5$  are shown in Fig. 12). There is quite a strong dependence in the initial distributions, but the differences are attenuated in the final distributions. The main reason is the slow overdamped evolution before scission which makes the evolution quasi-adiabatic and so less dependent on the initial conditions. Nevertheless, the difference in the final angular momenta for  $D_0 = 14$  and  $15.5$  fm are 20%. We may be taken as the model uncertainty at a quantitative level.

## VI. IMPACT OF OCTUPOLE DEFORMATION

There is one unexpected qualitative observation that can be explained within the FHF approach. Namely, the experimental results generally favor higher angular momentum in a more strongly deformed fragment, but the data in Ref. [36] for  $A_H \simeq 144$  and  $A_L \simeq 96$  have the opposite behavior. Although the quadrupole deformation of  $^{144}\text{Ba}$  is small, that nucleus has a large pear-shaped de-

formation (octupole) at the scission point which affects its angular momentum content. This may be seen in Fig. 13 which shows the angular momentum distribution with and without taking into account the pear-shaped deformation. Both initial and final angular momenta are increased when octupole deformation is present. More precisely, the final average angular momentum increases from  $\langle L_H^2 \rangle^{1/2} = 9.3$  to  $10.9 \hbar$  when the calculation includes octupole deformation.

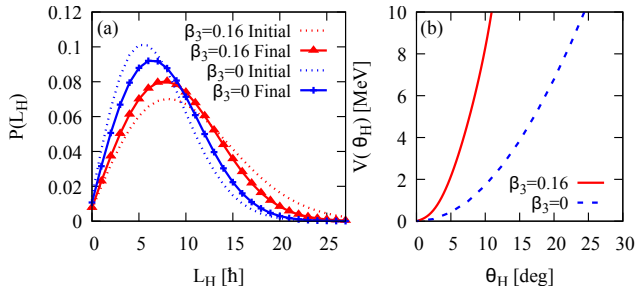


Figure 13. (Color online) Comparison with and without taking into account the octupole deformation. (a) Distribution of angular momentum at the initial and final time (b) Angular potential at a distance  $D=14$  fm. This calculation is done in one dimension, assuming a fixed light fragment with  $\theta_L = 0$ .

The effect is explained by the difference in stiffness of the angular potential as seen on panel (b). As shown in Ref. [42], the octupole deformation in the fission fragment minimizes the energy at the scission which promotes the production of fission fragments with an octupole deformation in their ground state. Here, the pear shape maximizes the nuclear interaction between the fragments at  $\theta_H=0$  and creates a stiffer potential at small angles. The stiffer potential induces a larger initial angular momentum.

## VII. CONCLUSION

The model presented here addresses the following questions regarding the collective contribution to the angular momentum generated in fission:

- What is the angular momentum distribution in the fission fragments?
- What correlations exist between the angular momenta of the two fragments?
- How does it depend on the Hamiltonian dynamics in the various states of the scission process?

In presenting the model conclusions it should be remembered that the model ignores the neck dynamics and cannot provide complete answers. First of all, the nuclei are considered to be cold in the sense that quasi-particle excitations are not included. These excitations also carry angular momentum and will augment it. Also, those exci-

tations may couple to the collective component, allowing the Coulomb moments to damp out with time. Obviously, this mechanism would decrease the post-scission contribution.

The most easily grasped observable in this study is the total angular momentum generated in each fission fragment. We see from the examples that it depends strongly on the fragment deformation and most of the angular momentum is present at an early stage, arising from the quantum uncertainty between angular momentum and orientation angle. While normally a large deformation would permit larger angular momentum, a surprising finding is that the lightly deformed  $^{144}\text{Ba}$  emerges with a higher angular momentum than its partner fragment due to an octupole deformation. A second finding is that the angular momentum gained in the post-scission evolution is of the order of 1-3  $\hbar$ . The gain is insensitive to the MOI of the fragments, unlike the initial angular momentum which decreases with the MOI.

Our analysis of the correlations between the angular momenta of the two fragments should provide a deeper insight into the effect of the potential at the scission point. There is hardly any correlation between the magnitudes of the angular momenta in the two fragments, in agreement with the experimental data of Ref. [3]. For the angular correlation between them, the potential favors V-shaped configurations that would correspond to bending mode vibrations and produce a negative angular correlation. We find that the correlations are small but positive, corresponding to a wriggling mode of vibration.

There are several ways the treatment of the neck-breaking could be improved. The Density-Constrained Hartree-Fock (Bogoliubov) [23–26] that contrarily to the FHF approximation does not violate the Pauli principle. Scission configurations could also be obtained from constrained calculations [43–45] or deduced from TDHF evolution [46]. The MOI of fragments could be obtained from a microscopic Hamiltonian [47]. Finally, the rotation of the fragments is not completely collective [22], which raises the question of how to simultaneously treat the collective and single-particle degrees of freedom [16, 48–53].

## ACKNOWLEDGMENTS

We thank the organizers A. Bulgac, J. Randrup, I. Stetcu, and J.N. Wilson as well as all the participants of the workshop on fission fragment angular momenta which led to interesting and inspiring discussions. And a particular thanks to Lee Sobotka for discussions at an early stage of the project. The funding from the US DOE, Office of Science, Grant No. DE-FG02-97ER41014 is greatly appreciated. This research used resources of the Oak Ridge Leadership Computing Facility, which is a U.S. DOE Office of Science User Facility supported under Contract No. DE-AC05-00OR22725.

- [1] M. Bender, *et. al.*, J. Phys. G: Nucl. Part. Phys. **47** 113002 (2020).
- [2] L. G. Moretto and R. P. Schmitt, Phys. Rev. C **21**, 204 (1980).
- [3] T. Døssing and J. Randrup, Nuclear Physics A **433**, 215-279 (1985).
- [4] J. Randrup and R. Vogt, Phys. Rev. Lett. **127**, 062502 (2021).
- [5] J. Randrup, T. Døssing, and R. Vogt, Phys. Rev. C **106**, 014609 (2022).
- [6] I. N. Mikhailov and P. Quentin, Physics Letters B **462**, 7–13 (1999).
- [7] L. Bonneau, P. Quentin, and I. N. Mikhailov, Phys. Rev. C **75**, 064313 (2007).
- [8] T. M. Shneidman, G. G. Adamian, N. V. Antonenko, S. P. Ivanova, R. V. Jolos, and W. Scheid, Phys. Rev. C **65**, 064302 (2002).
- [9] J. O. Rasmussen, W. Nörenberg, and H. J. Mang, Nucl. Phys. A **136**, 465-480 (1969).
- [10] M. Zielinska-Pfabé and K. Dietrich, Physics Letters B **49**, 123-128 (1974).
- [11] G. F. Bertsch, T. Kawano, and L. M. Robledo, Phys. Rev. C **99**, 034603 (2019).
- [12] P. Marević, N. Schunck, J. Randrup, R. Vogt, Phys. Rev. C **104** (2) L021601 (2021).
- [13] A. Bulgac, I. Abdurrahman, S. Jin, K. Godbey, N. Schunck, and I. Stetcu, Phys. Rev. Lett. **126**, 142502 (2021).
- [14] A. Bulgac, I. Abdurrahman, K. Godbey, and I. Stetcu, Phys. Rev. Lett. **128**, 022501 (2022).
- [15] N. Schunck and D. Regnier, Progress in Particle and Nuclear Physics, **125** 103963 (2022).
- [16] J. W. Negele, Rev. Mod. Phys. **54**, 913 (1982).
- [17] P. Ring and P. Schuck, *The Nuclear Many-Body Problem*, Texts and Monographs in Physics (Springer-Verlag, New York, 1980).
- [18] Marvin M. Hoffman, Phys. Rev. **133**, B714 (1964).
- [19] J. B. Wilhelmy, E. Cheifetz, R. C. Jared, S. G. Thompson, H. R. Bowman, and J. O. Rasmussen, Phys. Rev. C **5**, 2041 (1972).
- [20] Ş. Mişicu, A. Săndulescu, G. M. Ter-Akopian, and W. Greiner, Phys. Rev. C **60** 034613 (1999).
- [21] G.F. Bertsch, arXiv:1901.00928 [nucl-th] (2019).
- [22] G. Scamps, Phys. Rev. C **106**, 054614 (2022).
- [23] R. Y. Cusson, P.-G. Reinhard, M. R. Strayer, J. A. Maruhn, and W. Greiner, Z. Phys. A **320**, 475 (1985).
- [24] A. S. Umar, M. R. Strayer, R. Y. Cusson, P.-G. Reinhard, and D. A. Bromley, Phys. Rev. C **32**, 172 (1985).
- [25] G. Scamps and Y. Hashimoto, Phys. Rev. C **100**, 024623 (2019).
- [26] K. Godbey, A. S. Umar, and C. Simenel, Phys. Rev. C **106**, L051602 (2022).
- [27] C. Simenel, A. S. Umar, K. Godbey, M. Dasgupta, and D. J. Hinde, Phys. Rev. C **95**, 031601(R) (2017).
- [28] A. S. Umar, C. Simenel, and K. Godbey, Phys. Rev. C **104**, 034619 (2021).
- [29] K.-H. Kim, T. Otsuka, and P. Bonche, J. Phys. G **23**, 1267 (1997).
- [30] S. Goriely, J.-L. Sida, J.-F. Lemaître, S. Panebianco, N. Dubray, S. Hilaire, A. Bauswein, and H.-T. Janka, Phys. Rev. Lett. **111**, 242502 (2013).
- [31] J.-F. Lemaître, S. Goriely, S. Hilaire, and J.-L. Sida, Phys. Rev. C **99**, 034612 (2019).
- [32] A. Staszczak, A. Baran, J. Dobaczewski, and W. Nazarewicz, Phys. Rev. C **80**, 014309 (2009).
- [33] C. Simenel and A. S. Umar, Phys. Rev. C **89**, 031601(R) (2014).
- [34] A. Bulgac, P. Magierski, K. J. Roche, and I. Stetcu, Phys. Rev. Lett. **116**, 122504 (2016).
- [35] S. Franke-Arnold, S. M. Barnett, J. Leach, J. Courtial, and M. Padgett, New J. Phys. **6**, 103 (2004).
- [36] J.N. Wilson, D. Thisse, M. Lebois, et al. Nature, **590**, 566–570 (2021).
- [37] J. Randrup, , Phys. Rev. C **106**, L051601 (2022).
- [38] A. Bulgac, Phys. Rev. C **106**, 014624 (2022).
- [39] G. Scamps, I. Abdurrahman, M. Kafker, A. Bulgac, and I. Stetcu, arXiv.2307.14455 [nucl-th].
- [40] A. Bohr and B.R. Mottelson, Nuclear Structure Vol. II, (Benjamin,Reading,1975).
- [41] I. Stetcu, A. E. Lovell, P. Talou, T. Kawano, S. Marin, S. A. Pozzi, and A. Bulgac, Phys. Rev. Lett. **127**, 222502 (2021).
- [42] G. Scamps and C. Simenel, Nature volume **564**, 382-385 (2018).
- [43] J. F. Berger, J. D. Anderson, P. Bonche, and M. S. Weiss, Phys. Rev. C **41**, R2483 (1990).
- [44] M. Warda, J. L. Egido, L. M. Robledo, and K. Pomorski, Phys. Rev. C **66**, 014310 (2002).
- [45] R. Han, M. Warda, A. Zdeb, and L. M. Robledo, Phys. Rev. C **104**, 064602 (2021).
- [46] K. Washiyama, D. Lacroix, and S. Ayik, Phys. Rev. C **79**, 024609 (2009).
- [47] K. Washiyama, N. Hinohara, and T. Nakatsukasa, Phys. Rev. C **103**, 014306 (2021).
- [48] P. Arve, H. Reinhardt, Physics Letters B, **105**, 249-251,(1981).
- [49] D. Regnier and D. Lacroix, Phys. Rev. C **99**, 064615 (2019).
- [50] M. Verriere and D. Regnier, Front. Phys. **8**, 233 (2020).
- [51] A. Bulgac, S. Jin, and I. Stetcu, Phys. Rev. C **100**, 014615 (2019).
- [52] B. Li, D. Vretenar, T. Nikšić, P. W. Zhao, J. Meng, arxiv 2304.13369 (2023).
- [53] P. Marević, D. Regnier, D. Lacroix, arxiv 2304.07380 (2023).
- [54] See Supplemental Material at [URL will be inserted by publisher] for a program giving the internuclear potential.
- [55] See [dlmf.nist.gov/14.18](https://dlmf.nist.gov/14.18).
- [56] D.M. Brink and G.R. Satchler, *Angular Momentum* (Oxford University Press, Oxford 1962), Eqs. (4.17),(3.24), and last equation in App. II.

## Appendix A: Frozen Hartree-Fock potential, 1D case

The static potential has been obtained using the Frozen Hartree-Fock method on a grid of values of  $D$  and  $\theta$ . Solving the collective Hamiltonian model requires a finer grid. Then, a fit has been done of the FHF potential with the following form, with a separation of Nucleus-Nucleus interaction  $V_{NN}(\theta, D)$  and the Coulomb interac-

tion  $V_C(\theta, D)$ ,

$$V_{NN}(\theta, D) = \frac{V_0(D)}{1 + \exp\left(\frac{-|\sin(\theta)|^{0.5} - t_0(D)}{a}\right)}, \quad (\text{A1})$$

$$V_C(\theta, D) = \frac{e^2 Z_H}{2D^3} P_2(\cos(\theta)) Q_2^C + \frac{e^2 Z_H}{2D^5} P_4(\cos(\theta)) Q_4^C, \quad (\text{A2})$$

with,

$$V_0(D) = \exp(V_{0a}D^2 + V_{0b}D + V_{0c}), \quad (\text{A3})$$

$$t_0(D) = t_{0a}D^2 + t_{0b}D + t_{0c}. \quad (\text{A4})$$

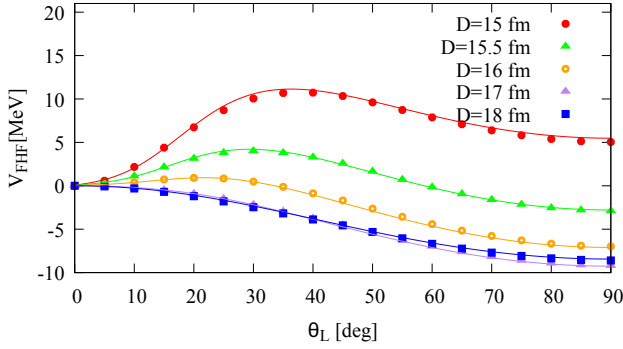


Figure 14. (Color online) Comparison between the Frozen Hartree-Fock potential (symbol) and the fitted potential eq. (A1) (lines) in the reaction  $^{240}\text{Pu} \rightarrow ^{132}\text{Sn} + ^{108}\text{Ru}$ .

Table III.

Variable	Sn+Ru	Ba(no oct.)+Sr	Ba(oct.)+Sr
$a$	0.1	0.13	0.106
$V_{0a}$ [MeV]	-0.1776	-0.1604	-0.1548
$V_{0b}$ [MeV]	4.117	3.660	3.673
$V_{0c}$	-18.76	-15.87	-16.56
$t_{0a}$	0.00609	0.	0.00393
$t_{0b}$	-0.2174	0.	-0.143
$t_{0c}$	2.501	0.82	1.903
$Q_2^C$ [fm <sup>3</sup> ]	614.5	276.14	299.88
$Q_4^C$ [fm <sup>5</sup> ]	12483.4	3907.63	23007.7

The values in the case of  $^{132}\text{Sn} + ^{108}\text{Ru}$  and simplified  $^{144}\text{Ba} + ^{96}\text{Sr}$  with fixed  $^{96}\text{Sr}$  with and without octupole deformation are shown on Table III. To test the validity of that parametrization a comparison between the FHF and the fitted potential is shown in Fig. 14.

### Appendix B: Frozen Hartree-Fock potential, 3D case

In the case of the  $^{144}\text{Ba} + ^{96}\text{Sr}$  the same angular grid has been used for the FHF calculation and in the collective Hamiltonian model. Rather than publishing the

very large table of entries for  $\hat{V}$  we provide in the Supplementary Material [54] a Fortran program to evaluate the four-dimensional internuclear potential. It has been checked that this potential leads to the same results as the original FHF one (See Fig. 15). In the Schrödinger code to evolve the wave function, nuclear matrix elements are interpolated as a function of  $D$  from computed values on a grid of spacing of 0.5 fm between  $D = 14$  and  $D = 17$  fm and 1 fm between  $D = 17$  and  $D = 20$  fm. For the other values of  $D$  the matrix elements are interpolated assuming an exponential evolution from the two closest existing matrix elements.

The Coulomb potential is parametrized as

$$V_C(\theta_H, \theta_L, D) = \sum_{l=2}^4 \frac{e^2}{2} \left( \frac{Z_L}{D^{l+1}} P_l(\theta_H) Q_{lH}^C + \frac{Z_H}{D^{l+1}} P_l(\theta_L) Q_{lL}^C \right). \quad (\text{B1})$$

The Coulomb moments are obtained by fitting the FHF Coulomb potential and are given in Tab. IV. These are close to the integrated values of Eq. (2).

Table IV. Parameters of the Coulomb moments

$Q_{2H}^C$	299.88 fm <sup>2</sup>
$Q_{2L}^C$	352.96 fm <sup>2</sup>
$Q_{3H}^C$	1453.96 fm <sup>3</sup>
$Q_{3L}^C$	0 fm <sup>3</sup>
$Q_{4H}^C$	9153.18 fm <sup>4</sup>
$Q_{4L}^C$	4849.29 fm <sup>4</sup>

### Appendix C: Angular momentum and torque

The angular momentum  $L$  in a system is changed by a torque in both classical and quantum mechanics, but the torque induced by the post-scission Coulomb field on the fragment's angular momentum is somewhat subtle. In this section, we derive analytic formulas for the time dependence of  $L$  to see why the net post-scission increase is quite small and dependent on the moment of inertia. The analysis proceeds with a generalization of Ehrenfest's theorem to relate the expectation value of the torque to the rate of change of angular momentum,

$$\frac{d}{dt} \langle \hat{L} \rangle = \frac{1}{i\hbar} \langle [\hat{L}, \hat{H}] \rangle. \quad (\text{C1})$$

Here  $\hat{L}$  and  $\hat{H}$  are operator in the space of orientation angles  $\theta$  and  $\varphi$ , and the brackets denote expectation values with respect to the instantaneous wave function. The commutator on the right is the quantum mechanical torque. The Hamiltonian  $\hat{H}$  is given by

$$\hat{H} = \frac{1}{2I} \hat{L}^2 + a P_2(\cos(\theta)) \quad (\text{C2})$$

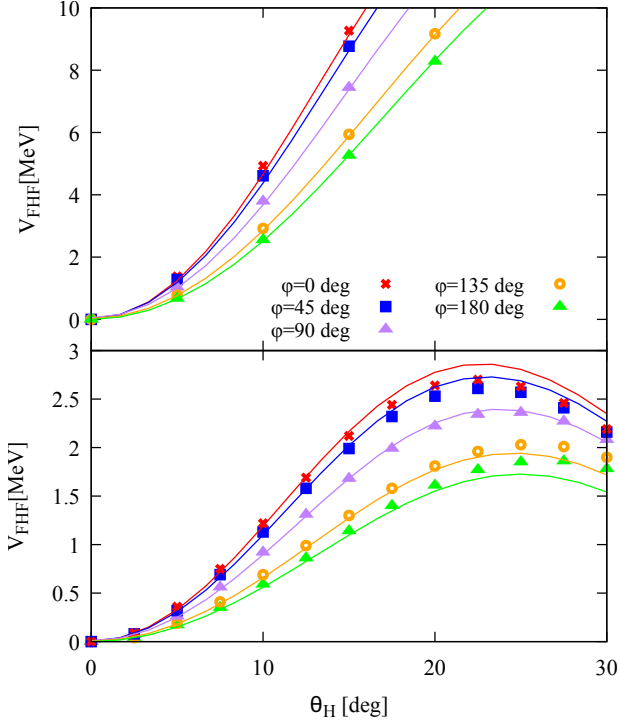


Figure 15. (Color online) Comparison between the Frozen Hartree-Fock potential (symbol) and the fitted potential eq. (A1) (lines) for  $D=15.5$  fm and  $D=16.5$  fm.  $\theta_L=\theta_H=25$  degrees.

where  $a = ZQ_f/(D(t))^3$  in Eq. (A2). The Hamiltonian commutator with  $\hat{L}_x$  evaluates to

$$[\hat{L}_x, \hat{H}] = -3i \cos(\theta) \sin(\theta) \sin(\varphi). \quad (\text{C3})$$

Notice that the torque is negative in the range  $0 < \theta < \pi/2$ , positive in the range  $\pi/2 < \theta < \pi$ , and zero at the endpoints of these intervals. This is just what one expects for a classical torque about the  $x$ -axis from a force derived from a potential that is symmetric under reflection in the  $xy$  plane. For example, the wave function  $\Psi(\theta, \varphi) \sim (\cos(\theta) + \sin(\theta)) \sin(\varphi)$  peaks in the  $yz$  plane at an angle  $\theta = \pi/4$ . It would be subject to a nonzero torque in the  $x$  direction.

The torque on the orientation of a fission fragment does not affect the angular momentum in the same way. The expectation value of the torque vanishes because the wave function's probability distribution is independent of the azimuthal angle  $\varphi$ . To understand this, note that  $|\Psi(\theta, \varphi)| = |\Psi(\theta, \varphi + \pi)|$ , so the contributions at both points will cancel. However, the Coulomb field still manages to increase the angular momentum content even when the probability distribution is axially symmetric. The change is not visible in  $\langle \hat{L}_x \rangle$  or  $\langle \hat{L}_y \rangle$  but rather through the squared total angular momentum in the  $xy$  plane,  $\hat{L}_x^2 + \hat{L}_y^2$ . For convenience, we assume a wave packet independent of  $\varphi$ , and we cast the polar angular variable

from  $\theta$  to  $\mu = \cos(\theta)$ ,

$$\hat{L}_x^2 + \hat{L}_y^2 = -\frac{\partial}{\partial \mu}(1 - \mu^2) \frac{\partial}{\partial \mu}. \quad (\text{C4})$$

Its commutator with the angular part of the Coulomb field is given by

$$[\hat{L}_x^2 + \hat{L}_y^2, P_2(\mu)] = -3 + 9\mu^2 + 6(\mu^3 - \mu) \frac{\partial}{\partial \mu}. \quad (\text{C5})$$

The commutator is a real anti-Hermitian operator so its diagonal matrix elements in real-valued wave functions are zero. Thus there is no change in  $L^2$  for the initial wave function as we have constructed. The wave function becomes complex during the time evolution due to the kinetic operator that changes the relative phases of the  $L$  components. This links the change in angular momentum to the moment of inertia. Smaller moments of inertia allow the relative phases of the components to build up more quickly, allowing the early transient Coulomb field to play a stronger role.

In the reaction producing  $^{108}\text{Ru}$  ( $\beta_2 = 0.82$ ), the Coulomb excitation plays an important role due to the large deformation of the fragment. As a result, the average angular momentum increases from  $9.3 \hbar$  at the scission to  $12.3 \hbar$  in the final state. This result shows the importance of the fission dynamics since a part of the angular momentum is generated in the Coulomb reorientation phase.

#### Appendix D: The angle of the fission axis

In general, the wave function of the collective model depends on an additional angle, namely the solid angle  $(\theta_f, \varphi_f)$  of the fission axis in the overall center-of-mass frame (CMF). We assume in our Hamiltonians that this angle is redundant provided that the overall angular momentum of the fissioning nucleus is zero. In this Appendix, we outline how this can be proved for calculating  $V_{NN}$  in the single-angle model.

First of all, the opening angle  $\theta_{ab}$  between two axes in terms of their angles in the CMF frame is given by

$$\theta_{ab} = \arccos(\cos \theta_a \cos \theta_b + \sin \theta_a \sin \theta_b \cos(\varphi_a - \varphi_b)) \quad (\text{D1})$$

where  $(\theta_i, \varphi_i)$  are the spherical coordinates of an axis  $i$  in the CMF. Then, with the help of the identity [55] we can write the spherical harmonic  $Y_{L0}(\theta_{ab})$  as

$$\begin{aligned} Y_{L0}(\theta_{ab}) &= \left(\frac{4\pi}{2L+1}\right)^{1/2} \sum_M Y_{LM}(\theta_a, \varphi_a) Y_{LM}^*(\theta_b, \varphi_b) \\ &= (4\pi)^{1/2} [L_a L_b]^0 \end{aligned} \quad (\text{D2})$$

where  $[L_1, L_2]^{L_3}$  is the usual notation for coupled angular momenta. The matrix element  $\langle L_1 | Y_{L_{ab}} | L_2 \rangle$  in the

single-angle representation can then be expressed in the CMF by using the above identity for each of the spherical harmonics. After carrying out some angular momentum algebra [56], the integral over the fission axis separates

out and can be evaluated analytically. The result is identical to the evaluated matrix element in the single-angle representation.